Coupled Fluid-Structural Characteristics of Actuators for Flow Control

by

Ruben Rathnasingham

Submitted to the Department of Aeronautics and Astronautics
in partial fulfillment of the requirements for the degree of

Master of Science in Aeronautics and Astronautics

at the

MASSACHUSETTS INSTITUTE OF TECHNOLOGY

September 1995

Author_____

Department of Aeronautics and Astronautics
Sept, 1995

Certified by_____

Professor Kenneth S. Breuer
Assistant Professor
Thesis Supervisor

Accepted by_____

Professor Harold Y. Wachman
Chairman, Departmental Committee on Graduate Students

Coupled Fluid-Structural Characteristics of Actuators for Flow Control

by

Ruben Rathnasingham

Submitted to the Department of Aeronautics and Astronautics
on Sept, 1995, in partial fulfillment of the
requirements for the degree of
Master of Science in Aeronautics and Astronautics

Abstract

The characteristics of two actuator designs for flow control are discussed. Both devices are based on resonating structures that interact with a closed volume of fluid to create a concentrated jet. The resulting unsteady flow through a small orifice introduces viscous effects that are characterized by the Stokes' parameter based on the orifice diameter. An optimum operating Stokes' parameter is then computed by matching this viscous dominated solution to an ideal, inviscid result. The actuators are modeled with a system of equations that describe their fluid-structural behavior. These models are compared to experimental results and are seen to predict time and frequency characteristics well. Experimental data also show that away from the exit orifice, the jet is self similar and its intensity is also governed by the Stokes' parameter. Scaling arguments are presented regarding actuator performance as a function of device size and Reynolds number in a turbulent flow. These arguments suggest that, in order to maintain adequate resolution at a given flow Reynolds number the device size must scale with the local momentum thickness.

Thesis Supervisor: Professor Kenneth S. Breuer
Title: Assistant Professor

Acknowledgments

I am grateful to numerous collegues and friends for their support and encouragement through these years of research. In particular, I would like to acknowledge the guidance and patience of my supervisor, Kenny. It's quite amazing how much I've learnt from him. Also, my former collegue Beth, with whom I spent many fun-filled hours in and out of work. She became a most trusting and devoted friend whom I'll remeber with the fondest of memories. Finally, my parents and my little sister who were always there when I needed them - at least via an international phone call !

Contents

List of Figures

Chapter 1

Introduction

Interest in active flow control for drag or noise reduction, flow vectoring, etc., has stimulated the recent development of innovative actuator designs that create localized disturbances in a flow field. A family of such actuators utilizes the large displacements attainable when structural members are driven at their resonant frequencies. These resonating structures are used to create pressure fluctuations in a closed cavity with an opening through which fluid is driven and used as a control input. Due to the relatively small sizes and high natural frequencies of the devices, off-resonance forcing will not provide sufficient deflections for control.

A design, referred herein as the 'Membrane' actuator, is illustrated schematically in Figure 1-1a. It was first proposed by Coe *et al.* [2] and consists of a thin membrane, rigidly fixed at its edges and driven into transverse oscillations at its resonant frequency. The membrane makes up an end wall of a closed, cylindrical cavity. The opposite wall is rigid and contains a small orifice. As the membrane deflects to compress the fluid in the cavity, the rise in pressure drives fluid out through the orifice. The outflow separates at the edge of the orifice and emerges as a normal jet. When the membrane deflects in the opposite direction, the orifice acts as a sink and fluid is drawn into the cavity from all directions. The differences between the inflow and outflow results in a time-averaged flow field resembling a vortex ring over the orifice with a steady jet emanating outwards from its core. Coe *et al.* [2] fabricated an extremely efficient micro-machined actuator with orifice diameters of 150-300 μm that achieved

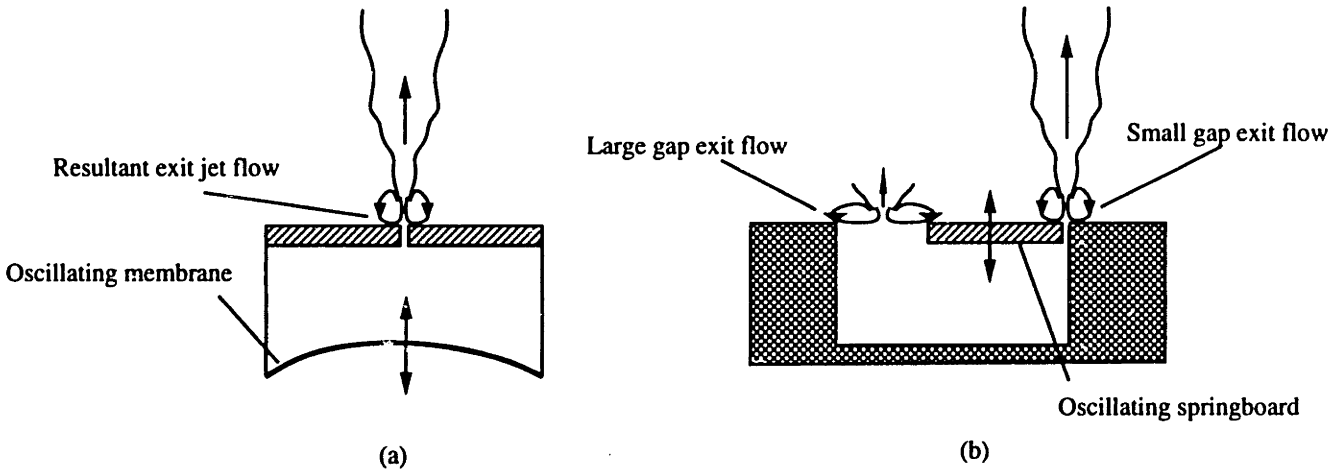

Figure 1-1: Schematic cross sectional views of the (a) 'Membrane' and (b) 'Springboard' actuators, showing the resulting time-averaged flow fields.

jet velocities of 17 m/s and penetration depths of 500 orifice diameters. Similar devices were also used to achieve jet thrust vectoring. An experimental investigation of the turbulent jet produced by a similar macro-sized device has also been carried out by James *et al.* [6].

A second design, referred herein as the 'Springboard' actuator, was first proposed by Jacobson and Reynolds [3] and comprises a piezo-ceramic/metal shim bimorph cantilever, mounted eccentrically over an open cavity (Figure 1-1b). The design presented here is modified in that a structurally 'soft' region is made at the rigid end of the cantilever to obtain larger tip displacements. The cantilever is driven at resonance with an alternating voltage and the oscillatory cavity pressure created, in turn, drives an unsteady flow through the cavity gaps. The time-averaged flow field over the narrower gap resembles a pair of line vortices accompanied by a normal jet. Mass conservation requires that a much less intense flow develop over the larger gap. However, a lower limit to the small gap width was observed, at which the mass flow through the small gap vanishes. An array of devices has been used in series with shear stress sensors for transition and turbulence control [5] and has produced encouraging results. Saddoughi [8] is currently developing a larger 'Springboard' device to be used as a vortex generator for the control of boundary layer separation.

These devices, although characterized by a single frequency, may be driven with

amplitude modulated signals at frequencies to which the global flow is receptive [12]. In order to use these devices to their full potential, it is vital that their behavior be fully understood. The devices must be accurately characterized to obtain a transfer function between the input (voltage) and output (mass ejection). To that end, it is necessary to consider the fluid-structural coupling of each actuator configuration. In this paper, the structural and fluid characteristics of these actuators are investigated and suitable models are considered. These models are then used in the analysis of experiments carried out with the 'Membrane' actuator.

Chapter 2

Theory and Modeling

In order to gain insight into the mechanisms that govern the fluid-structural coupling associated with each actuator design, theoretical models are considered in this section. The analysis is separated into structural and fluids sections. For the structural analysis, the devices are modeled as simple bending beams and plates. A transendental equation is obtained and solved for the eigenvalues and eigenmodes of each configuration. In the fluids analysis, both devices are simply modeled as a cavity filled with a compressible fluid that is forced out through one or more exits due to a pressure difference created by the action of an oscillating piston. A set of differential equations may be written to describe the fluid properties both inside and outside the devices.

2.1 Structural Modeling

2.1.1 The 'Membrane' Actuator

The 'Membrane' device is modeled as a circular plate, rigidly clamped at its edge. The solution to this problem is well documented [1, 13] and the first two natural frequencies are given by,

$$\omega_{m1,2} = K_{1,2}\sqrt{\frac{Et^3}{12(1-\nu_p)m_a R^4}}, \tag{2.1}$$

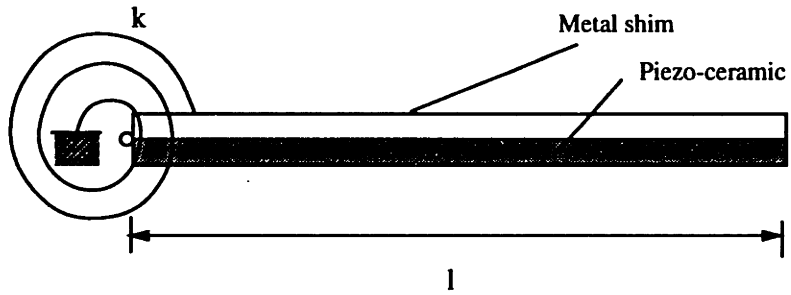

Figure 2-1: Structural model of the 'Springboard' actuator as a composite beam of length l, free at one end and supported by a spring of stiffness k, at the other.

Figure 2-2: Schematic of the 'Springboard' mode shapes for; (a) the first coupled mode (in phase) and (b) the second coupled mode (out of phase).

where $K_{1,2} = 10.2$ and 21.3, m_a, ν_p, t and R are the mass per unit area, Poissons' ratio, thickness and radius of the membrane, respectively. The mode shapes are given by [1],

$$\Phi_{1,2} = \left\{ J_{0,1}\left(\frac{K_{1,2}r}{R}\right) - \frac{J_{0,1}(K_{1,2})}{I_{0,1}(K_{1,2})} I_{0,1}\left(\frac{K_{1,2}r}{R}\right) \right\} \cos(i\theta), \tag{2.2}$$

where J_n and I_n are the Bessel functions and the modified Bessel function of the first kind of order n, respectively and r is the radial distance from the center of the membrane.

2.1.2 The 'Springboard' Actuator

The 'Springboard' device considered is different from that of Jacobson and Reynolds' [3] in that it has a low stiffness region at the fixed end. This was included because the highly rigid piezo-ceramic restricts the movement of the cantilever. In order to maximize its deflection, the cantilever is mounted with a small overhang, to ensure that most of the bending takes place in a small region near the fixed end. That is,

the piezo-ceramic extends from the tip of the cantilever to a short distance away from the fixed end, from where only the metal shim extends into the fixed support. This configuration creates a 'soft' point at the fixed end that allows much larger tip deflections. This configuration is modeled as a beam, free at one end, simply supported and connected to a spring at the other (Figure 2-1). Using energy methods with a three degrees of freedom system, the eigenvalues and mode shapes for the first two modes may be computed (Figure 2-2). The total kinetic energy, T, may be written as the integral of the time derivative of the cantilever displacement with respect to its length;

$$T = \frac{1}{2}\int_0^l m(z\dot{q}_1 + \phi_1\dot{q}_2 + \phi_2\dot{q}_3)^2\,dz \tag{2.3}$$

where m is the mass per unit length, q_1 is the spring angular displacement, $q_{2,3}$ are the first two degrees of freedom for a cantilever beam, l is the length of the cantilever, z is the distance from the fixed end and $\phi(z)_{1,2}$ are the functions that describe the first two mode shapes for a cantilever. Hence,

$$\begin{aligned} T &= \frac{1}{2}\int_0^l m(z^2\dot{q}_1^2 + 2z\phi_1\dot{q}_1\dot{q}_2 + 2z\phi_2\dot{q}_1\dot{q}_3 + 2\phi_1\phi_2\dot{q}_2\dot{q}_3 + \phi_1^2\dot{q}_2^2 + \phi_2^2\dot{q}_3^2)\,dz, \\ &= \frac{1}{2}I_0\dot{q}_1^2 + \int_0^l m(z\phi_1\dot{q}_1\dot{q}_2 + z\phi_2\dot{q}_1\dot{q}_3 + \phi_1\phi_2\dot{q}_2\dot{q}_3)\,dz + \frac{1}{2}\int_0^l m(\phi_1^2\dot{q}_2^2 + \phi_2^2\dot{q}_3^2)\,dz \end{aligned} \tag{2.4}$$

where I_0 is the mass moment of inertia of the cantilever, about its fixed end. The degrees of freedom are time-independent and may be excluded from the integrals. Thus, substituting M_{ij} for the integrals associated with products of $\dot{q}_i$ and $\dot{q}_j$, Equation 2.4 may be simplified to

$$T = I_0\dot{q}_1^2/2 + M_{12}\dot{q}_1\dot{q}_2 + M_{13}\dot{q}_1\dot{q}_3 + M_{23}\dot{q}_2\dot{q}_3 + M_{22}\dot{q}_2^2/2 + M_{33}\dot{q}_3^2/2. \tag{2.5}$$

Similarly, the total potential energy may be written as the total strain energy, U, in the cantilever:

$$U = kq_1^2/2 + M_{22}\omega_{0s2}^2q_2^2/2 + M_{33}\omega_{0s3}^2q_3^2/2 \tag{2.6}$$

where k is the spring stiffness and $\omega_{0s2,3}$ are the uncoupled fundamental and first harmonic frequencies for a cantilever. Using Lagranges' equation for each degree of freedom,

$$\frac{\partial}{\partial t}\left(\frac{\partial T}{\partial \dot{q}_i}\right) - \frac{\partial T}{\partial q_i} + \frac{\partial U}{\partial q_i} = 0, \tag{2.7}$$

leads to three coupled equations for $\mathbf{q}$, a column vector with elements q_1, q_2 and q_3:

$$\begin{Bmatrix} 1 & M_{12}/I_0 & M_{13}/I_0 \\ M_{12}/M_{22} & 1 & M_{23}/M_{22} \\ M_{13}/M_{33} & M_{23}/M_{33} & 1 \end{Bmatrix} \ddot{\mathbf{q}} + \begin{Bmatrix} \omega_{0s1}^2 & 0 & 0 \\ 0 & \omega_{0s2}^2 & 0 \\ 0 & 0 & \omega_{0s3}^2 \end{Bmatrix} \mathbf{q} = 0 \tag{2.8}$$

where $\omega_{0s1} = \sqrt{k/I_0}$, is the uncoupled spring natural frequency. The mode shapes for a cantilever beam are given by [11]:

$$\phi_n(z) = \cosh(\varepsilon_n z/l) - \cos(\varepsilon_n z/l) - \alpha_n(\sinh(\varepsilon_n z/l) - \sin(\varepsilon_n z/l)) \tag{2.9}$$

where $\varepsilon_{1,2} = 1.875$, 4.694 and $\alpha_{1,2} = .734$, 1.019, respectively. Finally, ϕ_n is normalized so that, $\int_0^l \phi_n^2\, dz = 1$. Assuming a harmonic solution, $q_j = \Re\{q_{0_j} e^{i\omega_s t}\}$, the transendental equation may be written:

$$\begin{aligned} &\left\{\frac{M_{13}^2 M_{22} + M_{12}^2 M_{33} + M_{23}^2 I_0 - 2M_{12}M_{23}M_{13}}{I_0 M_{22} M_{33}}\right\}\omega_s^6 \\ &+\left\{\left(1 - \frac{M_{23}^2}{M_{22}M_{33}}\right)\omega_{0s1}^2 + \left(1 - \frac{M_{13}^2}{I_0 M_{33}}\right)\omega_{0s2}^2 + \left(1 - \frac{M_{12}^2}{I_0 M_{22}}\right)\omega_{0s3}^2\right\}\omega_s^4 \end{aligned}$$

$$-\left\{(\omega_{0s1}\,\omega_{0s2})^2 + (\omega_{0s1}\,\omega_{0s3})^2 + (\omega_{0s2}\,\omega_{0s3})^2\right\}\omega_s^2 + \{\omega_{0s1}\,\omega_{0s2}\,\omega_{0s3}\}^2 = 0. \tag{2.10}$$

The spring natural frequency, is given by,

$$\omega_{0s1} = \sqrt{\frac{EI_1}{l' I_0}}, \tag{2.11}$$

where E is the Youngs' Modulus of the shim that extends into the support, I_1 is the first area moment of the shim alone and l' is the length of the cantilever not covered by the piezo-ceramic. Assuming that $l' \ll l$, beam bending theory [11] shows that,

$$\omega_{0s2} = 3.52\sqrt{\frac{EI_{eff}}{m_l l^4}}, \tag{2.12}$$

where EI_{eff} is the effective bending stiffness of the composite cantilever, m_l is its mass per unit length and

$$\omega_{0s3} = 22.03\sqrt{\frac{EI_{eff}}{m_l l^4}}. \tag{2.13}$$

The effective bending stiffness may be found by using the reference area method for a composite section.

Equation 2.10 may now be solved for the eigenvalues of the system, ω_s. Since the analysis was carried out to third order, the first two modes of the system may be obtained with accuracy.

2.2 Fluid Modeling

Fluid effects arise when the flexible structure causes a compression of the fluid in the cavity and when the unsteady flow that results from the unsteady cavity pressure, develops through the orifice. The model used is illustrated in Figure 2-3. The device is modeled as a piston of area A, moving in a cylinder of height H. The piston displacement normalized by the cavity height, x, is an average of the true membrane deflection described by Equation 2.2. The piston resembles the membrane, in that it causes an equivalent pressure change in the cavity. As the piston oscillates, the fluid in the cavity expands and compresses, leading to a fluctuating cavity pressure. Assuming the orifice area, a, is large enough that viscous effects are isolated at the boundaries and may be ignored, the cavity pressure change drives a flow through the orifice at a uniform velocity u. For smaller orifice diameters, viscous effects lead to a non-uniform velocity profile across the orifice and will be investigated in Section 2.3.

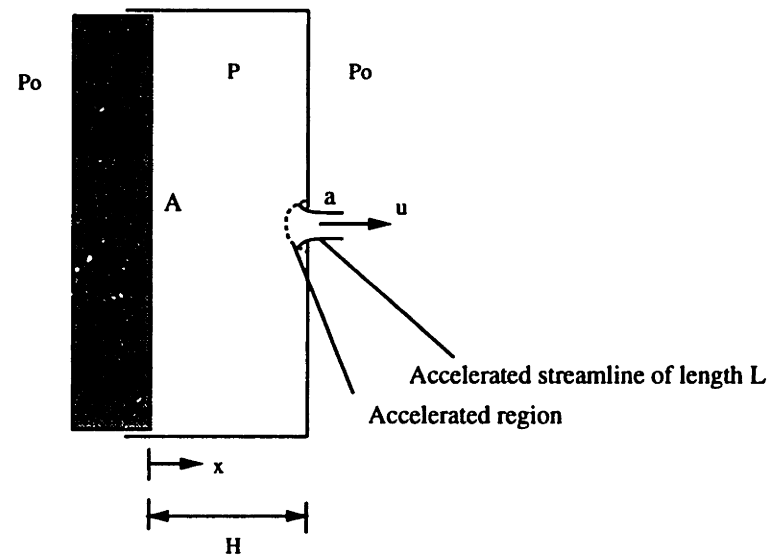

Figure 2-3: Features of the model for the analysis of fluid effects in a 'Membrane' actuator. The membrane is modeled as a piston of area A, that oscillates in a cavity from which flow is driven out through a small orifice of area a. The flow exit velocity, u, is assumed to be uniform and a nominal accelerating streamline, L, is assumed to stretch from a few diameters into the cavity to a few diameters into the emanating jet.

The 'Springboard' device is modeled in a analogous manner with the exception that there are two exit gaps (one on either side of the cantilever).

The modeling leads to two coupled equations for the density and jet velocity. The time derivative of the instantaneous mass in the cavity gives the rate of change of density as a function of the normalized membrane displacement and velocity and u:

$$\frac{\partial \rho}{\partial t} = \frac{\rho\left(AH\,\dot{x} - ua\right)}{AH\left(1-x\right)}. \tag{2.14}$$

Since the piston displacement is small compared to the cavity height, pressure fluctuations in the cavity are small and the jet exiting through the orifice is assumed to be subsonic and incompressible. Using the unsteady Bernoulli equation in streamline coordinates, the jet velocity may then be written in terms of the pressure difference across the orifice and a nominal accelerating streamline length, L:

$$\frac{\partial u}{\partial t} = \left(P - P_0\right)/\rho L - u\left|u\right|/2L \tag{2.15}$$

Since Equations 2.14 and 2.15 hold for any flow driven through a small opening, they are valid for both devices. The result of combining structural and fluid effects is summarized below as a set of five, coupled, non-linear first order differential equations with states that include the membrane position and velocity (x_1 and x_2), the fluid density and pressure and the jet velocity. The process is assumed to be isothermal. The forcing on the membrane is given by $G_0 \sin(\omega t)$.

$$\begin{aligned} \dot{x}_1 &= x_2 \\ M\dot{x}_2 &= -K_0 x_1 - C_0 x_2 - \frac{A}{H}(P - P_0) + \frac{G_0}{H}\sin(\omega t) \\ \dot{\rho} &= \frac{\rho(AH\,x_2 - ua)}{AH\,(1 - x_1)} \\ \dot{P} &= RT\dot{\rho} \\ \dot{u} &= (P - P_0)/\rho L - u\,|u|\,/2L \end{aligned} \tag{2.16}$$

where R is the universal gas constant, T is the fluid temperature, M is the mass of the membrane, K_0 and C_0 are the structural stiffness and damping coefficient, respectively. Equation 2.16 may be used as a transfer function to compute the actuator response. The structural stiffness and damping coefficients are dependent on the manufacturing technique and quality of the device and may be measured experimentally.

It is instructive to examine two limits for this system: (i) in which the cavity is sealed (i.e. $a \to 0$) and (ii) in which the fluid is incompressible. In the first case, the terms associated with the jet vanish and the entire system may be written as a single differential equation for the normalized membrane position, x:

$$M\ddot{x} = -K_0 x - C_0 \dot{x} - \frac{P_0 A\, x}{H\,(1 - x)} + \frac{G_0}{H}\sin(\omega t). \tag{2.17}$$

Expanding the compressibility term reveals that, for small values of x, the undamped natural frequency is given by

$$\omega_0 = \sqrt{\frac{K_0 + P_0 A/H}{M}}, \tag{2.18}$$

while for larger values of x, quadratic and cubic non-linearities will emerge resulting in the generation of harmonics and a modulation of the fundamental amplitude and a further shift in the natural frequency, proportional to x^2 [7].

For the second case - that of an incompressible flow - the conservation of mass reduces to a simple relationship between the piston velocity and the jet velocity:

$$u = \frac{AH}{a}\dot{x}. \tag{2.19}$$

This also results in a single differential equation for x:

$$(M + \rho_0 AL\frac{A}{a})\ddot{x} = -K_0 x - C_0\dot{x} - \rho_0 AH\left(\frac{A}{a}\right)^2 \frac{\dot{x}\,|\dot{x}|}{2} + \frac{G_0}{H}\sin(\omega t). \tag{2.20}$$

Here the non-linearities are more complex. On the left-hand-side of Equation 2.20 we see that there is an apparent mass term resulting from the unsteadiness of the fluid in the orifice. On the right-hand-side, a term proportional to $\dot{x}|\dot{x}|$ and $(A/a)^2$ acts as a fluid damping term. Note that as $a/A \to 0$, the term becomes singular due to infinite orifice velocities. In reality, the model is not valid in this limit since viscosity becomes dominant and restricts the mass flow through the hole. This is discussed in more detail in the following section. Expanding the $\dot{x}\,|\dot{x}|$ term in Fourier coefficients leads to linear and cubic damping terms, the second of which will result in a further source of frequency shift as the amplitude of the membrane oscillations increase. A full non-linear perturbation analysis of this rich system is currently underway.

2.3 The Stokes' Parameter

The preceding analysis on the fluid characteristics of the actuator was based on a uniform exit velocity, u. As the orifice size decreases, the viscous layer in the orifice grows, leading to a restriction in the the mass flow. Thus, at very small orifice sizes it is necessary to study the detail characteristics of the oscillating flow through the orifice. The orifice on a 'Membrane' device is circular, while the one on a large aspect ratio 'Springboard' device, may be considered to be a two dimensional slit.

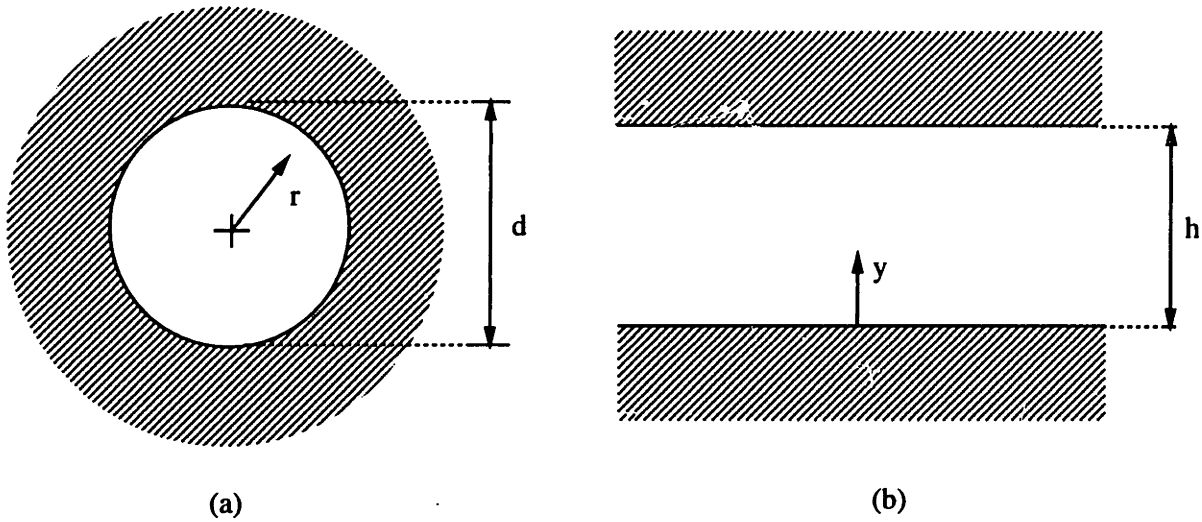

Figure 2-4: Coordinate system for the analysis of the Stokes' flow through; (a) a circular pipe of diameter d and (b) parallel plates separated by a distance h. Flow direction is normal to the page.

This problem is similar to the oscillating plate problem first examined by Stokes, except that now the solid boundary is stationary and the flow adjacent to it is driven by a pressure gradient, $\Pi_x(t)$, [10]. Viscous effects lead to a boundary layer in the orifice whose thickness is governed by the viscosity and the frequency of oscillation and may be expressed in terms of a Stokes' length scale, $l_S = \sqrt{\nu/\omega}$. There is a radially independent, potential flow velocity component, $u_p(t) = U\cos(\omega t)$, associated with the pressure gradient and it is necessary to find a velocity, $u_v(r,t)$ or $u_v(y,t)$ (in the case of the 'Membrane' and 'Springboard' devices, respectively), such that $u_p + u_v$ satisfies the no-slip boundary condition. The simplest form for u_v is given by the diffusion equation.

2.3.1 The 'Membrane' Model

The 'Membrane' problem is represented by an axisymmetric orifice and the diffu-

sion equation in cylindrical coordinates is given by,

$$\frac{\partial u_v}{\partial t} = \frac{\nu}{r}\frac{\partial}{\partial r}(r\frac{\partial u_v}{\partial r}). \tag{2.21}$$

Assuming a harmonic solution, $u_v(r,t) = \Re\{f(r)e^{i\omega t}\}$ and substituting into Equation 2.21 gives,

$$f = \alpha_m I_0(\sqrt{\frac{i\omega}{\nu}}r) + \beta_m K_0(-\sqrt{\frac{i\omega}{\nu}}r) \tag{2.22}$$

where α_m and β_m are arbitrary constants and K_0 is the complex Hankel function. Using the Stokes' parameter, $St_d = \sqrt{\omega d^2/\nu}$ and $\xi = 2r/d$ and boundary conditions,

$$\begin{aligned} f(0) &\text{ is finite,} \\ f(1) &= -U. \end{aligned}$$

adding on the contribution from u_p, the solution for $u(\xi,t) = u(\xi,t)_v + u_p$ is given by,

$$u(\xi,t) = \Re\left\{\frac{U\left(I_0(\sqrt{i}\,St_d\,\xi) - I_0(\sqrt{i}\,St_d)\right)}{(1 - I_0(\sqrt{i}\,St_d))}\,\exp(i\omega t)\right\}. \tag{2.23}$$

In the limit for small St_d, the flow is quasi-steady and u may be shown to approximate the Hagen-Poiseuille formula,

$$u(r,t) \approx \frac{\Pi_x}{4\nu}(d^2/4 - r^2). \tag{2.24}$$

2.3.2 The 'Springboard' Model

The 'Springboard' problem is approximated by a two dimensional slit and the diffusion equation gives,

$$\frac{\partial u_v}{\partial t} = \nu\frac{\partial^2 u_v}{\partial y^2}. \tag{2.25}$$

Assuming a harmonic solution, $u_v(y,t) = \Re\{f(y)e^{i\omega t}\}$ and substituting into Equa-

tion 2.25 gives,

$$f = \alpha_s \exp(\sqrt{\frac{i\omega}{\nu}}y) + \beta_s \exp(-\sqrt{\frac{i\omega}{\nu}}y) \tag{2.26}$$

where α_s and β_s are arbitrary constants. Imposing the no-slip condition at the wall and a symmetric velocity profile,

$$\begin{aligned} f(0) &= -U, \\ \frac{df}{dy}\left(\frac{1}{2}\right) &= 0. \end{aligned}$$

Using the Stokes' parameter and a non-dimensional length, $\eta = y/h$ and adding on the contribution of u_p, the solution may be written as,

$$u(\eta,t) = \Re\left\{U\left(1 - \frac{\{\exp(\sqrt{i}\,St_d\,\eta) + \exp(\sqrt{i}\,St_d(1-\eta))\}}{(1+\exp(\sqrt{i}\,St_d))}\right)\exp(i\omega t)\right\} \tag{2.27}$$

When St_d is large, the instantaneous velocity profile is uniform except for a viscous layer close to the wall. As St_d decreases, this layer grows until it penetrates the entire flow region. As St_d decreases further the flow is 'choked', that is the mass flow is reduced due to the effect of the viscous layer. Solving Equation 2.27 for the 'Springboard', the mass flow through the slit is seen to fall by 95 %, at $St_d \approx 1.5$. As St_d decreases further, the slit is essentially sealed and the mass flow appears across the larger gap. The 'Membrane' device behaves differently since the single orifice is the only way flow leaves and enters the cavity. In this case, the 'choking' phenomena leads to an effective stiffening of the membrane. This causes an increase in the fundamental frequency which in turn increases St_d so as to achieve the required mass flux. The effective thickness of the Stokes' layer is approximately $4\,l_S$ and $2.5\,l_S$ for the 'Springboard' and 'Membrane' devices, respectively. This corresponds to a critical St_d of 8 and 5, respectively, indicating that a 'Membrane' device could achieve a given jet velocity with a smaller exit hole.

Equations 2.24 and 2.27 describe the increase in the axial velocity as St_d increases and the solution for large St_d tends towards an asymptote defined by inviscid flow.

However, as the exit hole size increases (leading to an increase in St_d), mass conservation requires that the flow velocity should decrease proportionally to the hole area. Thus, matching these two regimes will provide an optimum St_d at which the maximum flow velocity is achieved for a given device.

Consider the solution for the 'Membrane' device. At small St_d, the axial velocity increases with d^2 or orifice area, a (Equation 2.24). When the boundary layer is restricted close to the orifice edge (at large St_d) so that the flow may be considered to be nearly inviscid, the axial velocity is then proportional the membrane velocity and inversely proportional to a (from mass conservation). Matching the center-line velocities in these two regimes requires:

$$\frac{\Pi_x a}{4\pi\nu} = \frac{AH}{a}\dot{x}.$$

Assuming a harmonic solution for the membrane deflection and substituting the expression for the fundamental frequency from Equation 2.1, one obtains, after some algebraic manipulation:

$$St_{opt} = 4\left(\frac{C^3 t_c H}{A^2 \pi^2 P_0 \nu}\right)^{\frac{1}{4}}, \tag{2.28}$$

where $C = K_1\sqrt{Et^3/(12(1-\nu_p)m_a)}$, as defined by Equation 2.1 and t_c is the orifice depth. St_{opt} is then the optimal Stokes' parameter for a given actuator design. It depends on the variation of the natural frequency with the device dimensions, cavity volume and depth of the orifice. St_{opt} for various actuator designs may be similarly computed if the natural frequency associated with the device is known.

Chapter 3

Experimental Techniques and Data Reduction

In order to test the theory presented in the previous section, experiments were carried out with relatively large devices. These macro-sized devices were more easily fabricated and manipulated allowing investigation of various configurations. Although much larger in size than would be practical for most flow control purposes, these devices provided a sufficient range of values of St_d for general conclusions to be drawn regarding their behavior with this parameter. The scaling of device size with flow parameters will be discussed in Section 4.5.

The 'Membrane' device shown in Figure 3-1 was made using a 170 μm thick brass shim bonded at its edge to steel washers. A small rectangular Nickel plated PZT-5H piezo-ceramic (250 μm thick) was bonded (using epoxy and silver paint) with one short edge rigidly fixed to the edge support. Since the purpose of the piezo-ceramic is only to excite the membrane at its resonant frequency, it may be small compared to the membrane size so as to minimize the interference on the motion of the membrane. In this case, it measured $R/4$ in length and $R/10$ wide, where R is the membrane radius. A reinforced cap was mounted over the support washer, creating a 1.2 mm deep closed cavity. The cap consisted of a 1 mm thick plexi-glass annulus sandwiched with a 250 μm brass shim. The jet exit hole was drilled through this shim, permitting an orifice flow. Hole diameters varied from 120 μm to 3.5 mm. Contact wires (24

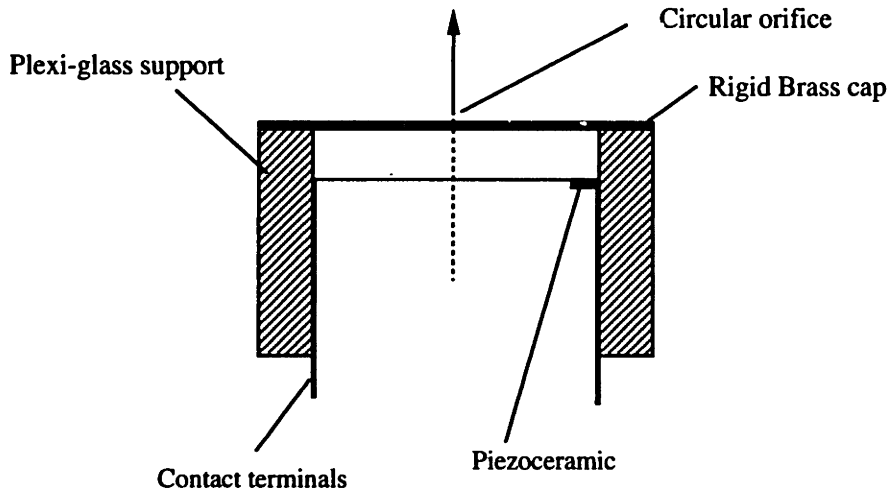

Figure 3-1: The circular symmetric 'Membrane' actuator is illustrated here in cross section, showing the position of the piezo-ceramic and contact wires.

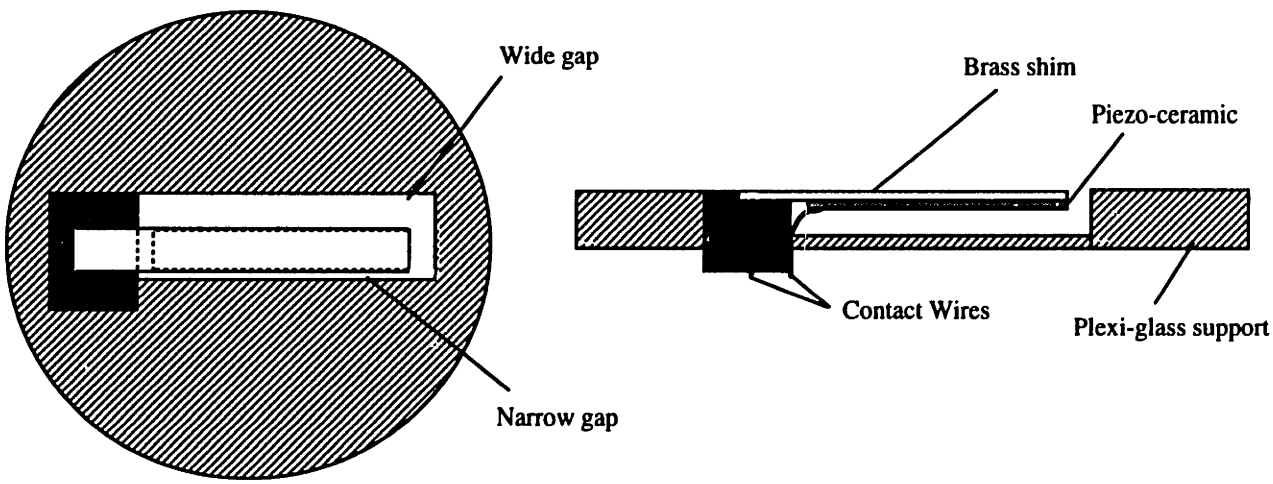

Figure 3-2: The 'Springboard' actuator shown eccentrically mounted over a cavity.

awg) were soldered onto the membrane and the ceramic.

The 'Springboard' bimorph, shown in Figure 3-2 was made up of a brass shim / piezo-ceramic sandwich (each 250 μm thick). The two materials were bonded together with epoxy and silver paint and then cut to size with a die saw. Wires were soldered onto the shim and piezo-ceramic. The cavity was cut out of a plexi-glass block. The bimorph was rigidly bolted to the plexi-glass support to form the springboard. Springboards were made 15 mm long and varied in width from 2 to 6.5 mm. The cavity size was fixed at 16 mm long, 7 mm wide and 2 mm deep.

Since both devices work on the same principal, a detailed study was first made with the 'Membrane' device and parallels were then drawn with the 'Springboard' device. In order to determine the structural characteristics of the actuators, an inductive sensor with a resolution of 5μm was used to measure the deflection of the springboard and membrane. Both actuator and sensor were held rigidly to a firm base so as to minimize structural vibrations. The measurements were made at the maximum deflection points for each actuator. The amplified signal from a digital function generator was used to provide the input to the devices. The dynamic response was measured using a sinusoidal sweep input about the resonant frequency of each device, which was obtained experimentally. The results were analyzed in terms of Bode plots. This procedure was carried out at different input voltages (from 5 to 90 V) in order to investigate amplitude characteristics and the linearity of the device response.

The jet characteristics of the device were investigated by using a constant temperature hot wire anemometer to measure the axial velocity component in the jet . The hot wire probe was traversed across the jet at different axial distances from the exit.

To minimize structural differences that arise during fabrication of the actuators, the membrane diameter was kept constant at 25.4 mm, while the jet exit hole diameter was varied from 120 μm to 3.5 mm, so as to obtain Stokes' parameters of 2.4 to 30.

Chapter 4

Results and Discussion

The frequency of the fundamental mode computed using Equations 2.1 and 2.10 agreed well with experimental data, with errors of less than 5 %, indicating that the 'Membrane' actuator behaves as a clamped circular plate and negligible interference was introduced by the piezo-ceramic. Also, this indicates that the 'Springboard' device behaves like a rigid beam supported by a spring at one end as modeled, that is, almost all the bending occurs at the fixed end to achieve larger tip deflections. A typical Bode plot for a 'Membrane' actuator with $St_d = 15.2$ is plotted in Figure 4-1 and shows an approximate second order behavior with a 180^0 drop in phase and a 20 dB/decade roll-off in magnitude. Thus the assumption of a second order equation of motion (Equations 2.20 and 2.17) is valid, at least to a first approximation and non-linearities are small and may be analyzed using perturbation theory.

The sharpness of the peak in the transfer function provides a measure of the damping in the system in terms of Q, the quality factor and its position provides the fundamental mode precisely. The Q corresponding to Figure 4-1 is 9 and indicates a lightly damped system (a non-dimensional, linear second order damping coefficient of 0.05).

The model described by Equations 2.16 was solved using a fourth order Runge-Kutta algorithm and the results matched experimental data well, as shown in Figure 4-2. The input was a burst of 100 periods at the fundamental frequency of 1750 Hz. By matching the rise and decay time of the membrane alone (that is, without

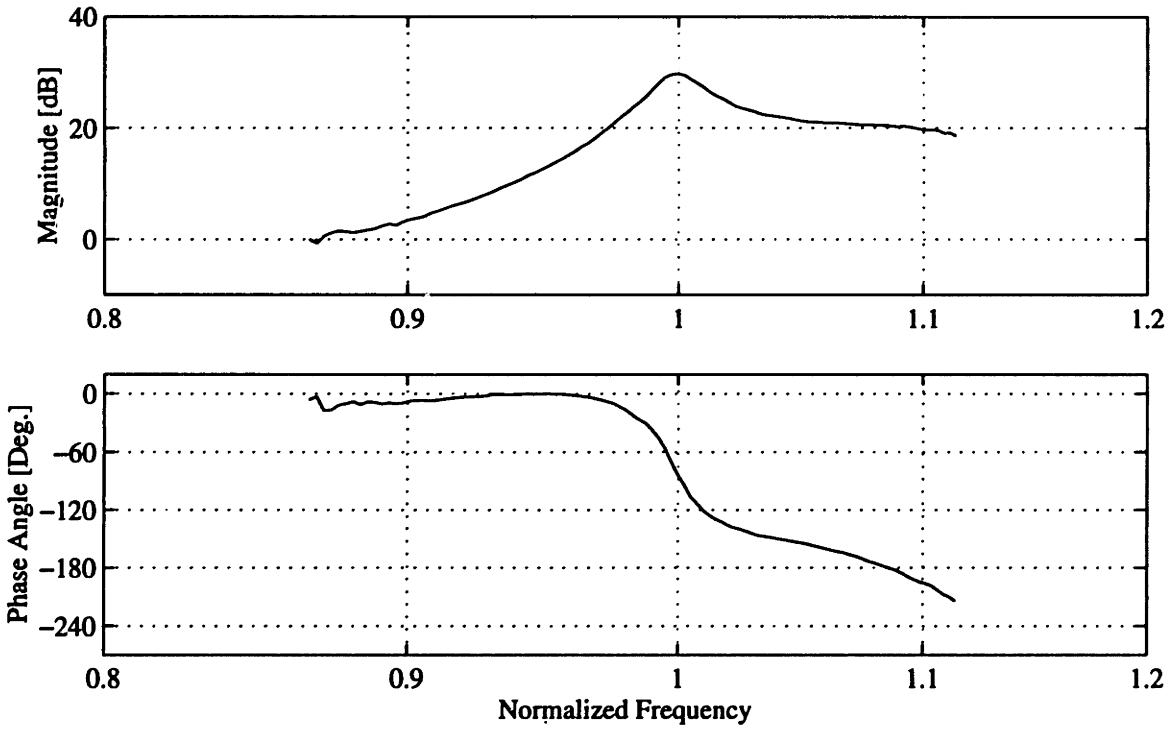

Figure 4-1: Bode plot of a typical 'Membrane' actuator response; $St_d = 15.2$, input amplitude of 20 V and fundamental frequency of 1750 Hz.

the closed cavity), it was possible to extract the structural stiffness and damping coefficients (in this case the stiffness, $K_0 = 120 \times 10^6$ N/m and the damping constant, $C_0 = 430$ Ns/m).

4.1 Non-Linear Characteristics

A plot of the transfer function at higher frequencies, indicates the existence of a super-harmonic mode at twice the frequency of the fundamental. Since no forcing was applied at the harmonic frequency, its magnitude was relatively small but was seen to grow with the square of the input amplitude (not shown). Phase information was noisy and unreliable. Cleaner data may be obtained if the system is forced at a single frequency corresponding to its fundamental mode. A sweep input, no matter how slowly modulated reduces the effective forcing at all frequencies. This has an effect on the absolute magnitude of the response but provides a true transfer function.

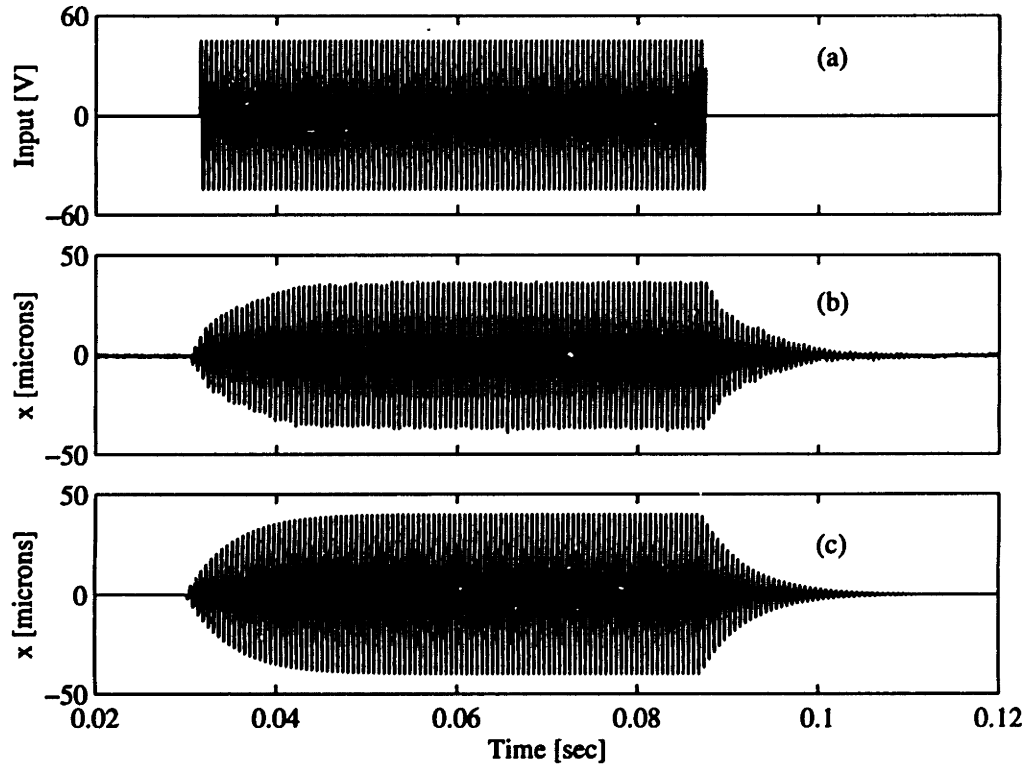

Figure 4-2: A typical burst input across the piezo-ceramic is shown in (a) and leads to a measured response (b), that may be compared to numerical results (c), for a 'Membrane' actuator. Experimental data corresponds to an actuator with $St_d = 15.2$, input amplitude of 20 V and fundamental frequency of 1750 Hz.

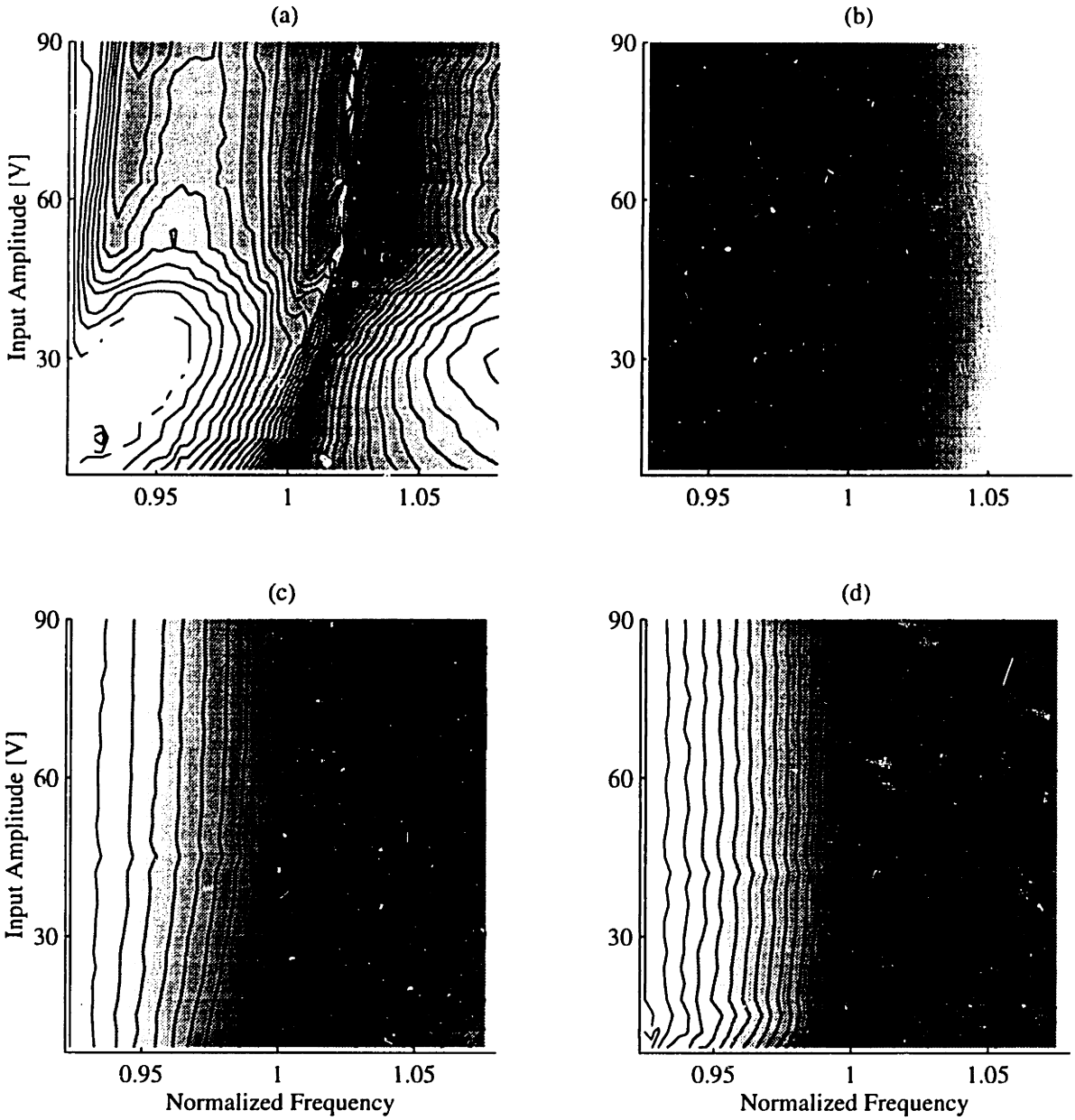

Figure 4-3: Contours of the transfer function amplitude for 'Membrane' actuators of various St_d; (a) Closed cavity ($\omega_0 = 1990Hz$), (b) $St_d = 3.5$ ($\omega_0 = 2000Hz$), (c) $St_d = 9.8$ ($\omega_0 = 1940Hz$) and (d) $St_d = 17.6$ ($\omega_0 = 1950Hz$) where ω_0 is the low-amplitude natural frequency. The transfer functions have been normalized for unity zero-frequency gain and contour line increments are identical for all plots. Darker shades correspond to higher values.

Thus, linear and non-linear system characteristics, namely fundamental frequency and amplitude, harmonic frequency and amplitude, damping and fundamental frequency shifts with input amplitude may be extracted from a contour or surface plot of the transfer function, plotted against frequency and input amplitude. Figure 4-3 is a series of such contour plots describing the behavior of the actuator with St_d and input amplitude. The contour line increments in each plot is identical.

When the cavity is fully sealed, (Figure 4-3a), the contour lines are closely spaced and there is a distinct increase in natural frequency with input amplitude and a modulation of the peak transfer function amplitude. This shift persists until an input amplitude of 50 V, above which the natural frequency remains constant. This behavior may be explained by considering the large fluid compression that introduces terms of order x^2 and x^3, which, from Equation 2.17, lead to a quadratic amplitude modulation and a shift in natural frequency with input amplitude, respectively. As the input amplitude rises to a critical value, the membrane displacement reaches a maximum (saturation) and its response is unchanged for higher input amplitudes. The closely spaced contour lines indicate that the stiffness term dominates here and damping is relatively light ($Q = 17$).

With a small exit hole (Figure 4-3b) corresponding to a St_d of 3.5, the contour lines are spaced much further apart and negligible frequency shift or amplitude modulation is observed. The transfer function peak amplitude is also smaller than that of the sealed case. This suggests that compressibility effects are negligible at the order of x^3. Furthermore, at this St_d the viscous layer penetrates the entire orifice area and reduces the mass flow through it so that non-linear terms associated with the unsteady jet velocity are also small. The reduction in the peak amplitude of the transfer function comes about from the large added mass term similar to that in Equation 2.20. The introduction of fluid damping through the orifice causes the increased separation between contour lines ($Q = 10$).

As St_d increases (Figure 4-3c), the contour lines move further apart and a pronounced frequency shift develops. Now, the viscous layer in the orifice diminishes so that larger unsteady velocities develop which strengthen the damping term in

Equation 2.20 that lead to a relatively large natural frequency shift. Note that the term associated with the unsteady jet also introduces added linear damping, whose effect is readily observed by the increased separation between the contour lines in the vicinity of the fundamental frequency and the reduction in the low-amplitude fundamental frequency ($Q = 6$). As the input amplitude increases, the peak transfer function amplitude rapidly rises to a maximum and remains constant, indicating that the dominant effect at this Stokes' parameter is that from the unsteady jet velocity.

At very large St_d (Figure 4-3d), the contour lines are more closely spaced and no frequency shift or amplitude modulation is observed. The relatively large orifice size eliminates the effect of fluid non-linearities and the flow may be considered to be effectively incompressible and inviscid. The shift in the natural frequency vanishes and the contour lines are more closely spaced, indicating that the reduced flow acceleration through the orifice makes the fluid damping term negligible ($Q = 9$). Furthermore, the peak transfer function amplitude remains constant.

Thus, the behavior of the actuator with St_d may be approximated by considering the limiting Equations 2.20 and 2.17 individually. In reality, there is an intermediate range of St_d where both effects apply simultaneously and coupling terms may arise. Further non-linear analysis is needed to obtain quantitative solutions in this range.

4.2 Jet Characteristics

Figure 4-4 illustrates the characteristics of the jet in terms of its mean and fluctuating center-line velocity and momentum thickness with respect to the non-dimensional axial distance from the orifice, x/d. Figure 4-4a shows that the center-line velocity accelerates to a maximum at $x/d \approx 10$, after which there appears to exist a jet whose mean velocity varies as x^{-1}. This behavior is indicative of an axisymmetric jet. For $x/d < 10$, the jet is not fully developed and as Figure 4-4c indicates, consists of large fluctuations that correspond to the oscillating membrane. Figure 4-4b describes the extent of the shear layer with streamwise distance and shows an initially large region of influence, followed by a rapid reduction up to $x/d \approx 10$. The layer then grows

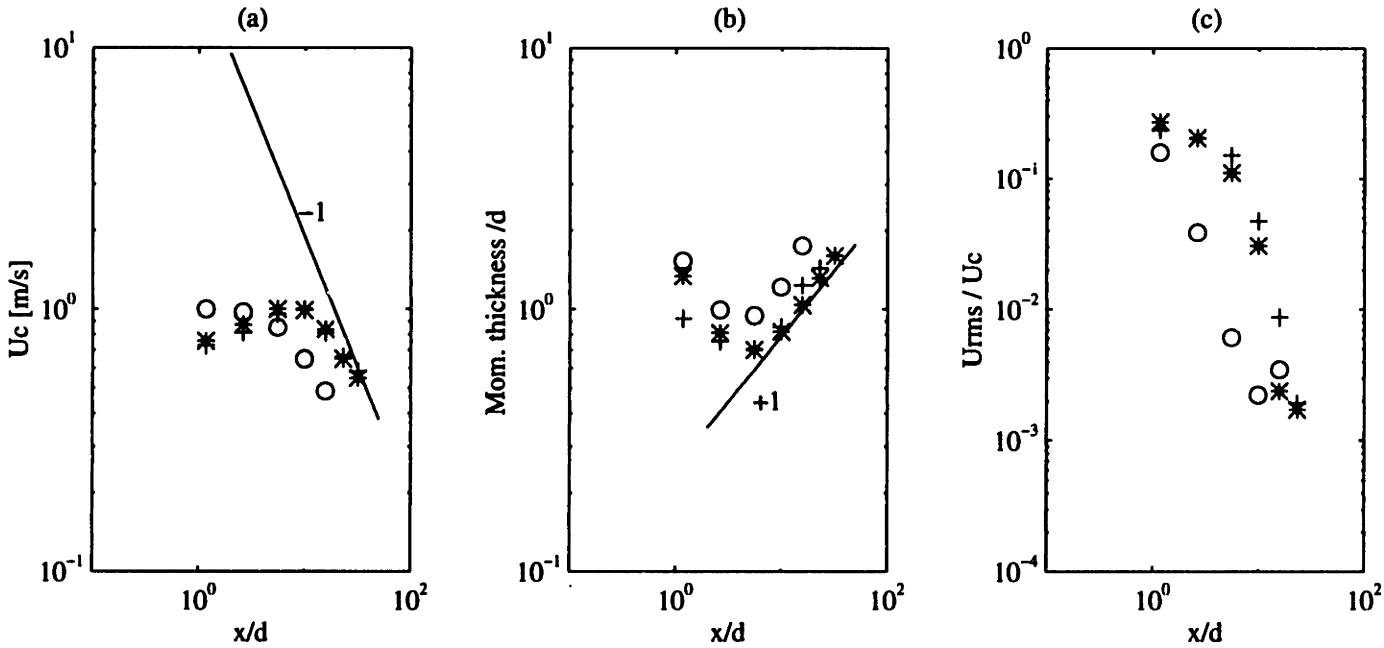

Figure 4-4: Jet characteristics plotted against x/d (a) U_c/U_{max}, (b) Jetwidth/d , (c) U_{rms}/U_c. Symbols indicate input amplitude; ○; 30 V, ∗; 60 V, +; 90 V. Solid lines indicates the behavior of an axisymmetric jet.

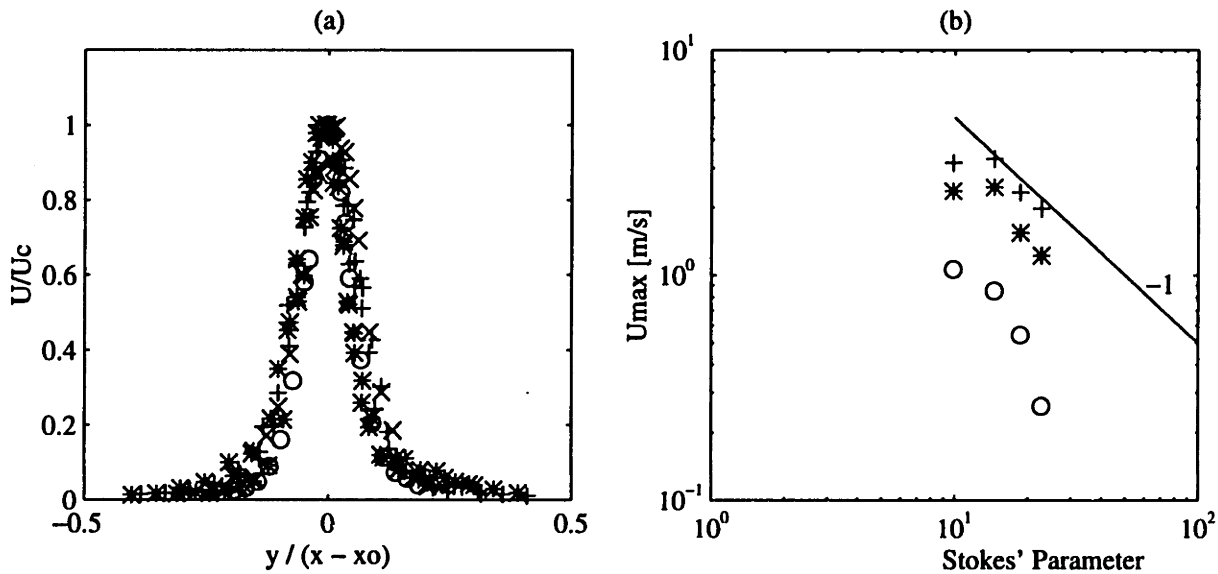

Figure 4-5: (a)Similarity profiles of the streamwise velocity component for $x/d > 10$, includes profiles for different input voltages (b) U_{max} scaling (solid line with a slope of -1 indicates incompressible theory).

linearly with x/d, again indicating the development of an axisymmetric jet. The results suggest that in the region close to the jet exit, a 'doughnut' shaped axisymmetric vortex structure surrounds the emanating jet, analogous to the longitudinal vortices observed by Jacobson and Reynolds [4]. This phenomena is caused by the irreversible unsteady orifice flow and its influence extends to the point where a stable, well developed jet can form. Figure 4-4c also shows the rapid decay of the fluctuating component with the streamwise distance which begins only after the coherent jet forms.

In Figure 4-5a, the jet velocity profiles for $x/d > 10$ are plotted in similarity coordinates. It clearly shows that the jet is similar in the outer region. Figure 4-5b is a plot of the maximum center-line velocity, which occurs at the beginning of the similar jet, against St_d. The plot indicates an optimum St_d of approximately 15, at which the actuator performs most efficiently (maximum Reynolds number of 150). This compares well with the optimum value of 16 predicted by Equation 2.28. Below this value, fluid non-linearities are dominant as discussed earlier and above this value, the flow is essentially incompressible and inviscid (solid line) and the velocity falls with increasing orifice diameter. This critical St_d corresponds well with what was observed in the Section 4.1 as the point where the flow may be considered to be essentially incompressible and inviscid.

4.3 Comparisons of the Springboard and Membrane Actuators

As mentioned previously, both devices work on the same basic principle. The key difference being that the 'Springboard' device has two gaps for fluid flow out of the cavity whereas the 'Membrane' device is restricted to having only one. Hence when St_d gets small enough for fluid effects to cause significant resistance, the 'Springboard' device allows fluid to flow through the larger gap, effectively sealing the narrow gap. Compressibility effects become negligible and the mean velocity, u, is prevented from

getting large enough for non-linear fluid effects to be present unless both gaps correspond to low St_d. Similar experiments carried out with the 'Springboard' actuator, show no natural frequency shift or super-harmonic growth, except at large input amplitudes where the structural deflections become large enough to cause non-linear effects. Furthermore, for St_d less than approximately 1.5, no jet flow could be detected over the narrow gap. Hot wire measurements were not made closer than 5 gap widths away from the exit and errors in measuring the gap width could lead to errors of $\pm 10\%$ in St_d.

4.4 Optimal Actuator Design

Taking into consideration the behavior of the actuators discussed here, a modified design for resonant actuators is proposed. It encompasses the benefits of both devices and utilizes some of the subtler fluid properties observed in an effort to increase efficiency. Figure 4-6 shows a schematic of the device. It is a cantilever mounted in a closed cavity with a slit at one end for the jet exit. The springboard is made, such that the gaps around it are small enough so that $St_d < 1.5$, making a seal. A hole made in the springboard is covered with a flexible membrane. This acts as a valve, allowing fluid to flow in on the down stroke but closing on the up stroke, enabling fluid to fill the cavity from an external source. This increases the efficiency of the device by reducing viscous loses across the exit slit. The external source of fluid also enables the use of a high concentration of devices without competition for the available fluid in the flow.

4.5 Scaling Arguments for Flow Control

For practical flow control purposes, the length, time and velocity scales of an actuator must be comparable to those associated with the flow so as to achieve full controllability. Scaling arguments regarding actuator performance may be developed for particular flow fields for which characteristic scales are well defined. The following

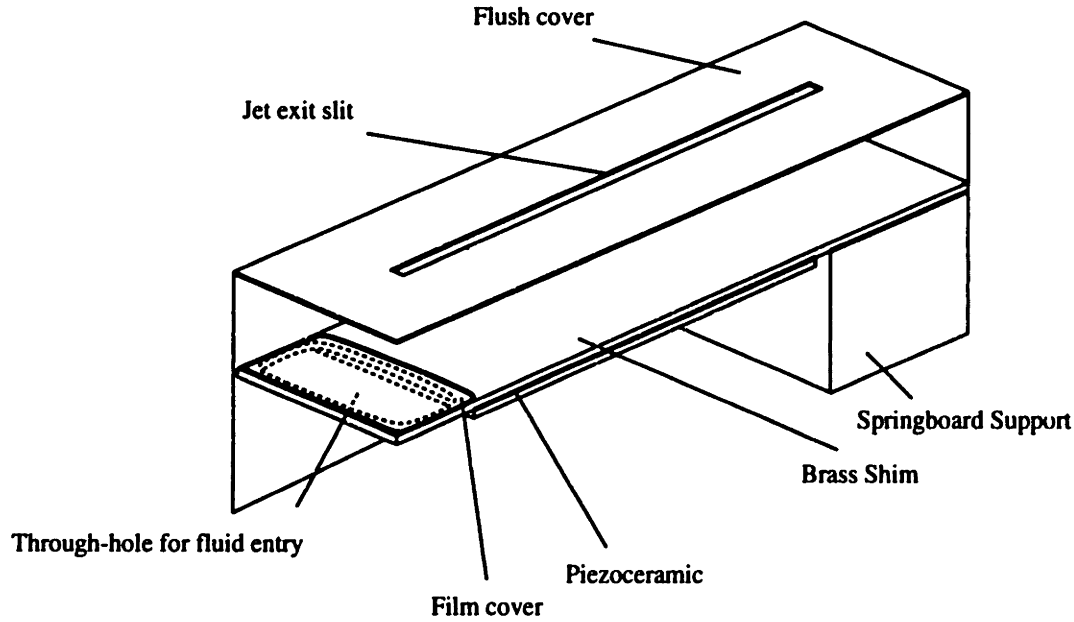

Figure 4-6: Proposed design for second generation actuator

approach develops an argument for turbulent flow control based on a fixed optimal Stokes' parameter.

In turbulent flow, fundamental flow structures scale with viscous lengths and times that, in turn, scale with the flow Reynolds number. To a first approximation, it may be shown [9] that the viscous length scale, l^*, varies as $\theta\, Re_\theta^{-9/8}$, times scale, t^*, varies as $\theta^2 Re_\theta^{-7/4}/\nu$ and the velocity scale, u^*, varies as $\nu Re_\theta^{5/8}/\theta$, where $Re_\theta = U_\infty \theta/\nu$ is the turbulent flow Reynolds number based on the local momentum thickness, θ, and the characteristic flow velocity, U_∞ .

Using the structural model developed in Section 2.1 and imposing a fixed St_d, scaling arguments may be made regarding actuator configuration in a turbulent wall flow. In particular, the characteristic length, time and velocity scales of the device normalized by corresponding turbulent quantities may be expressed in terms of a Reynolds number based on the local momentum thickness. The following analysis assumes a well fabricated 'Membrane' device with a high quality factor. The charac-

teristic length normalized with the viscous length scale may be written as:

$$d/l^* = d^* \sim \left\{\frac{\rho_a \nu^2}{Et^2}\right\}^{\frac{1}{4}} St_d \, Re_\theta^{9/8} \frac{D}{\theta}, \tag{4.1}$$

where ρ_a and D are the membrane material density and diameter, respectively. The first factor on the right hand side of Equation 4.1 is the parameter consisting of the device and fluid properties that imposes a given St_d. With both St_d and the flow Reynolds number specified *a priori*, it indicates that the membrane size is required to vary as the local momentum thickness in order to maintain a given resolution. Thus, if such devices were arranged on a large surface their sizes would vary with location to maintain adequate resolution.

In general, the response time of the control jet is several times the period of the forcing function (in the above experiments, an average of 10 cycles were needed before the steady state condition was reached). To maintain good control performance the ratio of the flow to device time scale must be much greater than unity and be kept at a relatively high value throughout all flow conditions. The characteristic time scale normalized by the viscous time scale may be written in terms of a turbulent Stokes' parameter:

$$\sqrt{\omega t^*} = \sqrt{\omega l^{*2}/\nu} = St^* \sim \left(\left\{\frac{\rho_a \nu^2}{Et^2}\right\}^{\frac{1}{4}} Re_\theta^{7/8} \frac{D}{\theta}\right)^{-1}. \tag{4.2}$$

Equation 4.2 indicates a similar linear relationship between device size and momentum thickness for time scales as for length scales.

The jet velocity will depend on the forcing method and amplitude. These factors influence the zero frequency membrane amplitude, x_0, and the cavity compression, respectively. An approximation may be made by assuming an incompressible flow and a circumferential forcing method. That is, the force is applied around the edge of the membrane (say, electrostatically [2]). In this case, the characteristic velocity normalized by a viscous velocity scale may be expressed in terms of the device and

fluid properties as follows,

$$u_{jet}/u^* \sim Q\, x_0 \left(\left\{ \frac{\rho_a \nu^2}{E t^2} \right\} St_d\, Re_\theta^{-5/8} \frac{D}{\theta} \right)^{-1}. \tag{4.3}$$

The quality factor of the device, Q, appears in Equation 4.3 because it is a measure of the maximum attainable amplitude, while the zero frequency amplitude gives an indication of the efficiency of the forcing method. The device size is again scaled with the local momentum thickness as a similarity parameter.

Chapter 5

Conclusions

A model for resonant fluid actuators that create an unsteady jet through the compression of a cavity was developed. It includes five coupled, non-linear state equations. Compressibility and unsteadiness are shown to lead to non-linear fluid effects that dominate when the jet exit size is small. The model was compared to experimental data and successfully predicted trends in the behavior of the 'Membrane' actuator. The Stokes' parameter based on the jet exit diameter is used to describe the behavior of the device and the results indicate that for this particular actuator configuration, $St_d \approx 15$ defines an upper boundary for fluid effects, above which, the jet characteristics is governed by incompressible theory . This critical value is accurately predicted by theory. It also defines the most efficient configuration for a given 'Membrane' actuator design.

A similar, axisymmetric jet is observed beyond 10 diameters away from the exit and sustains itself beyond 100 diameters. Close to the exit, the flow irreversibilities lead to a complex, vortical flow structure that could not be accurately investigated in this experiment. Scaling arguments for the device in a turbulent boundary layer indicates that the associated viscous lengths and times, scale with the flow Reynolds number and the local momentum thickness.

Bibliography

[1] R.D. Blevins. *Formulas for Natural Frequency and Mode Shape.* Krieger Publishing Company, Malabar, Florida, 1984.

[2] D.J. Coe, M.G. Allen, M.A. Trautman, and A. Glezer. Micromachined jets for manipulation of macro flows. *Solid-State Sensor and Actuator Workshop*, pages 243–247, 1994.

[3] S.A. Jacobson and W.C. Reynolds. A piezoelectric actuator for controlling turbulent flows. *Status Report, Stanford University*, 1993.

[4] S.A. Jacobson and W.C. Reynolds. Active boundary layer control using flush mounted surface actuators. *Bull. Am. Phys. Soc.*, 38(9), 1994.

[5] S.A. Jacobson and W.C. Reynolds. Active control of transition and drag in boundary layers. *Bull. Am. Phys. Soc.*, 39(9), 1994.

[6] R.D. James, J.W. Jacobs, and A. Glezer. Experimental investigation of a turbulent jet produced by an oscillating surface actuator. *Proceedings of the Twelfth US National Congress of Applied Mechanics*, pages S127–S131, 1994.

[7] A.H. Nayfeh. *Nonlinear Oscillations.* John Wiley & Sons, New York, New York, 1979.

[8] S.G. Saddoughi. Experimental investigations of 'on-demand' vortex generators. *Annual Research Briefs, Center for Turbulence Research*, pages 197–203, 1994.

[9] H. Schlichting. *Boundary Layer Theory.* McGraw-Hill, Inc, New York, New York, 1968.

[10] F.S. Sherman. *Viscous Flow.* McGraw-Hill, Inc, New York, New York, 1968.

[11] S. Timoshenko and S. Woinowsky-Kreiger. *Theory of Plates and Shells, 2nd ed.* McGraw Hill, New York, New York, 1959.

[12] R.D. Wiltse and A. Glezer. Manipulation of free shear flows using piezo actuators. *J. Fluid Mech.*, 249:261–285, 1993.

[13] W.C. Young. *Roark's Formulas for Stress & strain, 6th ed.* McGraw Hill, New York, New York, 1989.